Zhang *et al. Carbon Research* (2026) 5:11
https://doi.org/10.1007/s44246-025-00255-z

Carbon Research

ORIGINAL ARTICLE

Open Access

Lignin-derived hierarchical porous carbons enabling high-voltage electrochemical capacitors with low self-discharge

Shichao Zhang[1†], Shenglin Liu[2†], Suyang Si[1], Keqi Zeng[1], Chenxin Cai[1], Xiangzhou Yuan[2,3], Yawen Tang[1], Feng Gong[2*] and Hualin Ye[1*]

Abstract

The widespread deployment of electrochemical capacitors in energy-intensive technologies is fundamentally limited by their low energy density and severe self-discharge. The search of high-voltage supercapacitors has the appeal of an effective solution to increase the energy density, but suffers from risk of electrolyte decomposition and self-discharge. We herein address this challenge through a synergistic electrode/electrolyte co-design that integrates a lignin-derived porous carbon electrode with a tailored Li^+-based weakly solvating electrolyte containing a functional fluorinated diluent. The porous carbon features sub-nanometer pores that are geometrically matched to the weakly solvated Li^+ ions, enabling stable operation at an unprecedented 4.0 V with a high energy density of 77.4 Wh kg^{-1} and over 90% capacitance retention after 10,000 cycles. Mechanistic analysis reveals that the sub-nanometer pores precisely accommodate solvated ions to facilitate high capacitance, while the fluorinated diluent suppresses electrolyte degradation and mitigates parasitic reactions under elevated potentials.

Highlights

- A porous carbon electrode with a precisely tailored pore architecture was synthesized from sustainable lignin-derived biomass.
- Integration of this porous carbon with a weakly solvating electrolyte affords a capacitance of 139 F g^{-1} and stable operation at 4.0 V.
- This synergistic design achieves a high energy density of 77.4 Wh kg^{-1} and long cyclability with 90% of its capacitance after 10,000 cycles.

Keywords Lignin, Carbon, Weakly solvating electrolyte, Supercapacitor, High-voltage

---

†Shichao Zhang and Shenglin Liu contributed equally to this work.

*Correspondence:
Feng Gong
gongfeng@seu.edu.cn
Hualin Ye
hualin@njnu.edu.cn
Full list of author information is available at the end of the article

Graphical Abstract

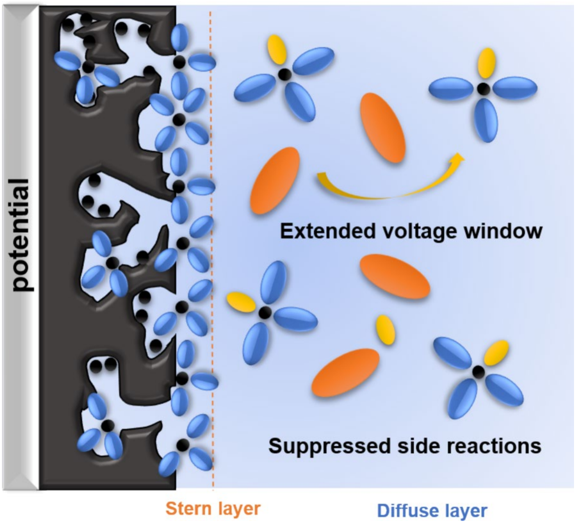

1 Introduction

Electric double layer capacitors (EDLCs) offer outstanding power density and long cyclability, yet their application in energy-intensive applications is hindered by their inherently low energy density and pronounced self-discharge (Chun et al. 2015). Since the energy density scales quadratically with the operating voltage window, increasing this voltage window has emerged as one of the most effective solutions for enhancing energy density (Pech et al. 2010). For instance, extending the voltage window from the typical 2.7 V (*i.e.*, the commercial standard) to 4.0 V could theoretically increase the energy density by more than 120%. Unfortunately, this promise is restricted by the electrochemical instability of conventional electrolyte systems (Fig. 1a). Aqueous systems are limited to ≈1.2 V due to water decomposition, while non-aqueous electrolytes—typically based on tetraethylammonium tetrafluoroborate ($TEABF_4$) in acetonitrile (AN) and propylene carbonate (PC)—undergo degradation beyond 2.7 V (Lu et al. 2024), resulting in electrolyte decomposition and severe self-discharge.

To address these challenges, two main strategies have been pursued. The first involves the use of solvents with intrinsically high electrochemical stability, such as ionic liquids (ILs). For instance, 1-butyl-3-methylimidazolium trifluoromethanesulfonate (BMIMOTf) could enable a high operation voltage window to ~3.5 V (Kumar et al. 2020). However, this approach is severely hampered by the high viscosity of ILs, which hinders ion transport and lowers power density (Ren et al. 2018). The second strategy relies on the use of high- concentration electrolytes (HCEs) (Ho et al. 2023), in which the reduced activity of free solvent molecules extends the electrochemical stability window up to 4.0 V (Yuan et al. 2024). Unfortunately, HCEs suffer from drawbacks similar to ILs, including excessive viscosity and high material costs. Moreover, the high concentration salt in HCEs can intensify parasitic redox reactions at the electrode surface, causing rapid capacity fading and aggravated self-discharge (Zhang et al. 2023; Ye and Li 2023).

Recently, weakly solvating electrolytes have been actively pursued for developing high-voltage electrolyte systems for batteries (Zhong et al. 2015). These electrolytes typically consist of electrolyte salts dissolved in solvents in the presence of non-coordinating or weakly coordinating diluents. They are characterized by significantly faster ion desolvation kinetics compared to conventional nonaqueous electrolytes, owing to the intentionally weakened interaction between charge-carrying ions and solvent molecules (Kim et al. 2023). By facilitating this desolvation process, weakly solvating electrolytes can enhance ion transport kinetics and improve charge storage efficiency, presenting as a promising pathway to overcome the high-viscosity limitations associated with both ILs and HCEs (Blasio et al. 2024).

Encouraged by these advantages, we herein developed a high-voltage electrolyte for supercapacitors based on the weakly solvating principle (Fig. 1b). The electrolyte comprises alithium salt (tetrafluoroborate, $LiBF_4$), a high-oxidation-stability solvent (sulfolane, SUL), and

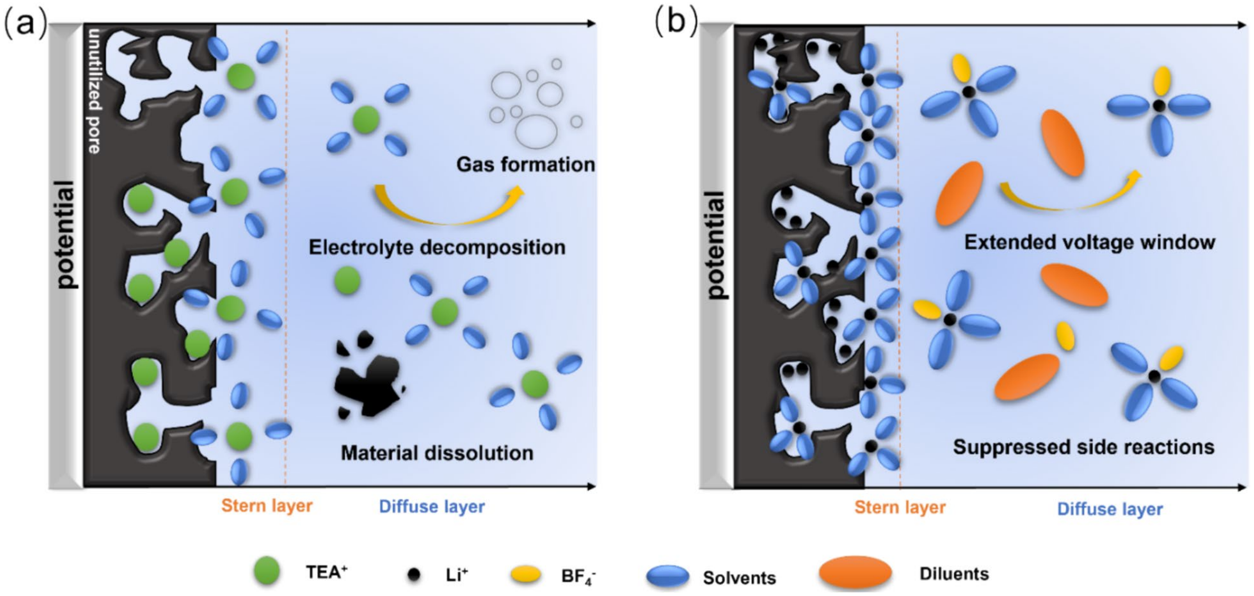

Fig. 1 Schematic illustration of the electric double layer of porous carbon electrodes at elevated potentials in **a** a conventional electrolyte and **b** a weakly solvating electrolyte

1,1,2,2-tetrafluoroethyl-2,2,3,3-tetrafluoropropyl ether (TTE) as a functional non-solvating diluent. This formulation is synergistically paired with a hierarchical porous carbon derived from renewable lignin, featuring sub-nanometer pores ($\approx$0.8 nm) that are geometrically matched to the solvated Li^+ ion ($\approx$0.8 nm in SUL). Such a structural compatibility enables a high specific capacitance of 139 F g^{-1} and a stable 4.0 V operating window with excellent cycling stability, giving rise to a large energy density of 77.4 Wh kg^{-1} that is far beyond most conventional EDLCs reported to date. Notably, the addition of TTE diluents creates a unique interfacial environment that effectively suppresses parasitic side reactions, affording a markedly reduced self-discharge rate compared to conventional electrolyte systems.

2 Materials and methods

2.1 Materials preparation

2.1.1 Materials

Lignin was supplied by Linyi Senhe Biomaterials Co., Ltd. (Linyi, China). All chemical reagents, including potassium hydroxide (KOH, 95%), polytetrafluoroethylene (PTFE, 99%), tetraethylammonium tetrafluoroborate ($TEABF_4$, 99%), lithium tetrafluoroborate ($LiBF_4$, 99.9%), and the diluent 1,1,2,2-tetrafluoroethyl-2,2,3,3-tetrafluoropropyl ether (TTE, 99.5%), were purchased from Aladdin Holding Group Co., Ltd. (Beijing, China) and used as received, sulfolane (SUL, 99.9%) was purchased from Duoduochem, Acetylene black (Super P) was procured from Shenzhen Kejing Zhida Technology Co., Ltd. (Shenzhen, China). Deionized water was used for all washing and solution preparation steps.

2.1.2 Preparation of lignin-derived hierarchical porous carbon (HPC)

Lignin and KOH were thoroughly ground at a mass ratio of 1:2 and transferred into a tube furnace. The mixture was then heated to 250 °C at 5 °C min^{-1} and held for 1.5 h under N_2 flow, followed by a ramp to 800 °C (3 °C min^{-1}) for 2 h to finish the carbonization process. After natural cooling to room temperature, the resulting product was ground and washed sequentially with deionized water (6 h) and 1 M HCl (6 h) to remove residues. The obtained solid was then repeatedly rinsed with deionized water until the filtrate reached neutrality (pH $\approx$ 7), and finally dried in a vacuum oven at 120 °C for 12 h.

2.1.3 Preparation of electrolytes

Five electrolyte systems were prepared in an argon-filled glovebox ($O_2 < 0.1$ ppm, $H_2O < 0.1$ ppm) to ensure anhydrous conditions. For the 1 M $LiBF_4$/SUL, 9.38 g of $LiBF_4$ (molar mass: 93.75 g/mol) was precisely weighed and dissolved in 80 mL of anhydrous sulfolane. The mixture was heated to 60 °C with magnetic stirring for 20 min to facilitate complete dissolution. For the 1 M tetraethylammonium tetrafluoroborate/propylene carbonate [$TEABF_4$/PC], 17.36 g of $TEABF_4$ (molar mass: 217.06 g/mol) was precisely weighed and dissolved in 80 mL of anhydrous propylene carbonate (PC). This mixture was heated to 60 °C with magnetic stirring for 20 min to ensure full and uniform dissolution. For the 1 M tetraethylammonium tetrafluoroborate/sulfolane [$TEABF_4$/SUL], a protocol consistent with the 1 M $TEABF_4$/PC was adopted: 17.36 g of $TEABF_4$ was precisely weighed, dissolved in 80 mL of anhydrous SUL, and heated to 60 °C with magnetic stirring for 20 min to achieve complete dissolution. The 4 M $LiBF_4$/SUL followed a similar protocol but with 37.50 g of $LiBF_4$ (4× molar amount), requiring 30 min of stirring at 60 °C to achieve homogeneity in the highly concentrated solution. For the 4 M $LiBF_4$/SUL:TTE = 1:2 composite electrolyte, 10 mL of the pre-prepared 4 M $LiBF_4$/SUL was mixed with 20 mL of TTE by volumetric ratio, manually shaken for 2 min to ensure miscibility without heating. All electrolytes were stored in sealed vials within the glovebox.

2.1.4 Fabrication of symmetric supercapacitors

To prepare working electrodes, the active material (commercial YP-50F or the prepared HPC) was blended with conductive agent (Super P), and binder (PTFE) with an 8:1:1 weight ratio, in an agate mortar. The mixture was then transferred to a 2 mL vibrating tube with an appropriate amount of deionized water and zirconia beads. The tube was subjected to high-speed oscillation for 180 s, repeated three times, to form a homogenous slurry. The resulting slurry was uniformly cast onto a piece of aluminum foil using a doctor blade with a gap height of 500 μm. The coated foil was then dried in a vacuum oven at 120 °C for 12 h to completely remove water and any residual volatiles. After drying, circular electrode discs with a diameter of 14 mm were punched from the coated foil. The active material loading on each electrode was controlled to be in the range of 2–3 mg cm^{-2}. Symmetric supercapacitors were assembled in CR2025-type coin cells inside an argon-filled glove box. The assembly consisted of two identical electrodes separated by a cellulose-based separator (NKK-MPF30AC-100), with stainless steel spacers and a spring to ensure proper pressure and electrical contact. For each cell, 40 μL of the designated electrolyte was added to ensure complete wetting of the electrodes and separator. After sealing, the assembled cells were allowed to rest for 12 h to allow for full electrolyte infiltration before electrochemical testing.

2.2 Electrochemical measurements

All electrochemical tests were performed on the assembled CR2025 coin cells at room temperature. Cyclic voltammetry (CV), linear sweep voltammetry (LSV), galvanostatic charge–discharge (GCD) were conducted using an AutoLab electrochemical workstation. Long-term cycling stability tests were carried out using a LAND CT2001A battery testing system. CV tests were performed at various scan rates from 10 to 100 mV s^{-1} within the specified voltage window for each electrolyte. The LSV measurements were conducted under an operating voltage ranging from 0 to 5.5 V, with lithium metal as both the reference and counter electrodes. GCD tests were conducted at different current densities ranging from 0.2 to 10 A g^{-1}. EIS measurements were performed in a frequency range from 100 kHz to 10 mHz with an AC voltage amplitude of 10 mV s^{-1}. Self-discharge tests were conducted by charging the cells to a specific voltage, holding for 1 h, and then monitoring the decay of the open-circuit voltage (OCV) over 48 h. Leakage current was measured by holding the cells at a constant voltage for 48 h and recording the steady-state current. The specific capacitance(Cs, in F g^{-1}) of a single electrode was calculated from the GCD curves using the formula: $Cs = (4 \times I \times \Delta t)/(m \times \Delta V)$, where I is the discharge current, Δt is the discharge time, m is the total mass of active material on both electrodes, and ΔV is the voltage window during discharge. Energy density (E, in Wh kg^{-1}) and power density (P, in W kg^{-1}) were calculated using the equations: $E = (Cs \times (\Delta V)^2)/(8 \times 3.6)$ and $P = (E \times 3600)/\Delta t$.

3 Results and discussion

The preparation of lignin-based HPC followed a general synthetic strategy via an activation-pyrolysis strategy. Lignin, a renewable industrial byproduct, is an ideal precursor for porous carbons due to its high carbon content, abundant aromatic ring structures, wide availability, and low cost. During the pyrolysis carbonization process, metallic potassium (K) and potassium-containing compounds (e.g., K_2CO_3 and K_2O), generated via the reaction between KOH and the carbon precursor, serve as potent etching agents that carve out a large number of micropores within HPC for enhanced specific surface area (Fig. 2a). Figure 2b illustrates the X-ray diffraction pattern (XRD) of the final products. The spectrum displays two broad and diffuse envelopes of peaks around ≈25.4 and ≈43.5° that are assignable to (002) and (110) diffraction of carbon. This feature reflects the non-crystallinity and highly disordered structure of HPC, consistent with the relatively higher D-to-G band intensity ratio ($I_D/I_G = 0.97$) observed in its Raman spectrum (Fig. 2c), compared to that of graphitic carbons (often < 0.3). Nitrogen adsorption–desorption analysis (Fig. 2d) was used to quantify the pore structure of HPC. The isotherm exhibits a combined Type I/IV character, with a sharp uptake at low relative pressures, indicative of abundant micropores, and a hysteresis loop at medium-to-high pressures, signifying the presence of mesopores. The specific surface area of HPC shows an impressive value of 2844 m^2 g^{-1}, nearly double that of commercial activated carbon

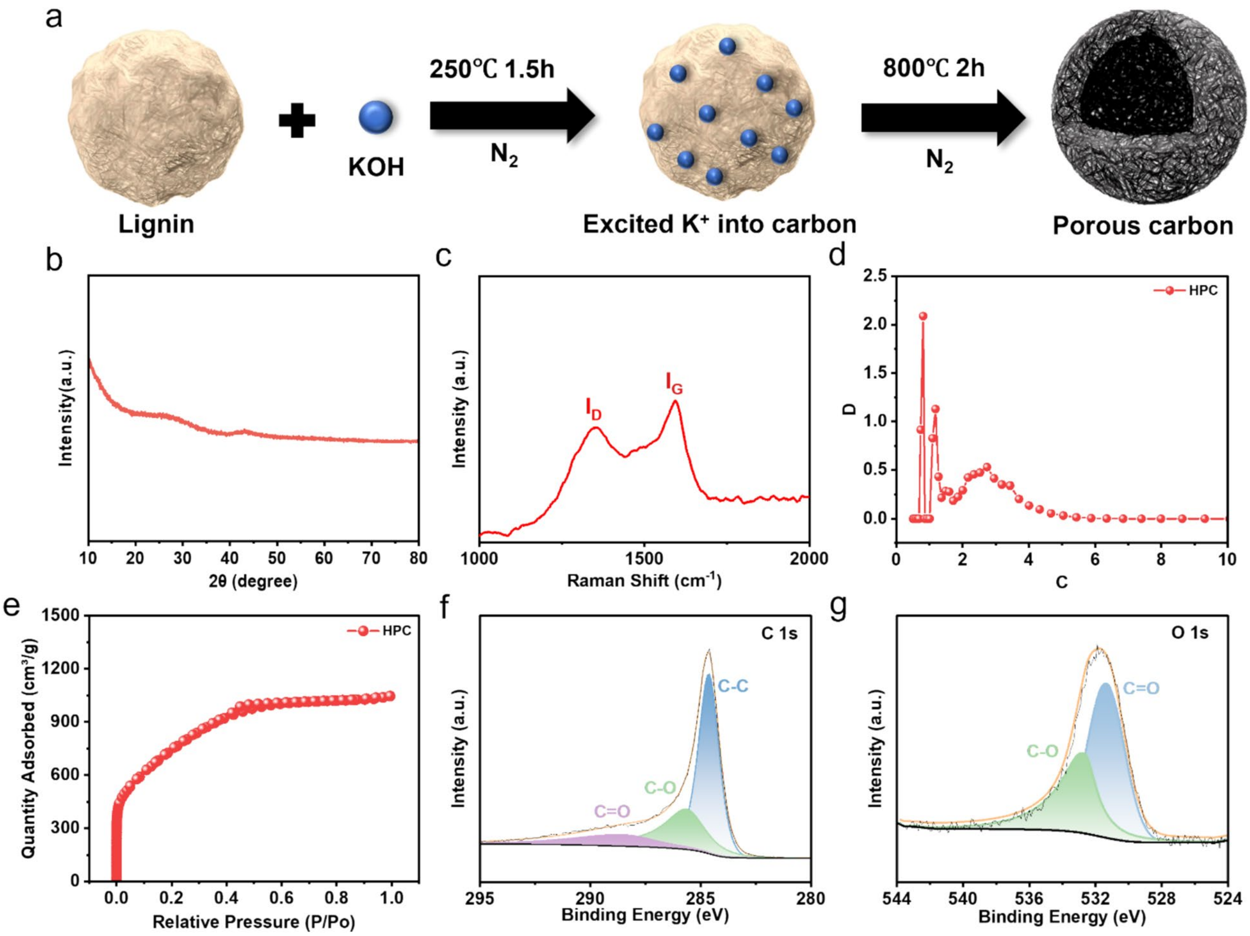

Fig. 2 Preparation and spectroscopic characterizations of HPC. **a** Synthetic route; **b** XRD pattern; **c** Raman spectra; **d** Nitrogen adsorption–desorption isotherm; **e** Pore size distribution; **f** C 1 s and **g** O 1 s XPS spectra

(Kuraray YP50, 1580 $m^2\ g^{-1}$) (Table S1; Pan et al. 2025; Zhang et al. 2021). As shown in Fig. 2e, HPC possesses a well-balanced hierarchical pore structure with a large population of sub-nanometer micropores (≈0.8 nm). By comparison, two additional HPC carbons were also prepared under identical synthesis conditions by changing the KOH-to-lignin mass ratios. Nitrogen adsorption–desorption analysis (Fig. S1) shows that decreasing the mass ratio to 1 (*i.e.*, insufficient activation, denoted as HPC_{insu}) results in smaller sub-nanometer micropores (≈0.6 nm) in HPC, while increasing the mass ratio to 3 (*i.e.*, excessive activation, denoted as HPC_{exce}) gives rise to broader pore size distribution from 1–8 nm. Their detailed pore parameters in comparison with commercial activated carbon (Kuraray YP50) were summarized in Table S1 (Pan et al. 2025; Zhang et al. 2021). X-ray photoelectron spectroscopy (XPS) analysis (Fig. 2f, g) confirms the presence of abundant oxygen-containing functional groups, such as C-O and C=O, on the carbon surface. These polar functionalities are beneficial for electrolyte wettability for a much easier ion penetration, as verified by contact angle measurements (Fig. S2).

To visually interrogate the macro/micro-structure of HPC, we next conducted morphological analysis using scanning electron microscopy (SEM). As shown in Fig. 3a and b, SEM images clearly reveal that the KOH activation process transformed the lignin precursor into a highly interconnected, three-dimensional (3D) porous network. This 3D open framework stands a stark contrast to the dense, granular morphology of commercial Kurary YP50F (Fig. S3), offering low-tortuosity, high-efficiency transport pathways for electrolyte ion diffusion. Energy-dispersive X-ray spectroscopy (EDS) elemental maps (Fig. 3c-e) further confirm the uniform distribution of carbon and oxygen throughout the carbon framework, which is in strong agreement

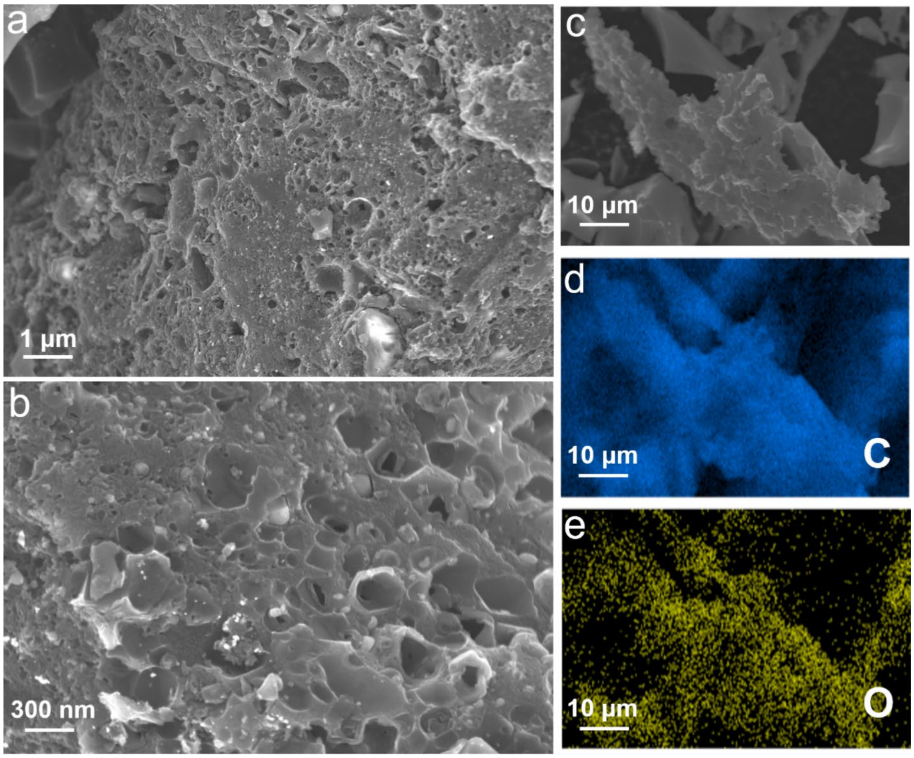

Fig. 3 **a**, **b** SEM images and **c**-**e** corresponding EDS elemental mapping showing the spatial distributions of C and O species

with the abundant oxygen heteroatoms surface chemistry analysis from XPS.

The electrochemical performance of HPC was assessed in symmetric capacitors with $LiBF_4$/$TEABF_4$ in SUL as the electrolyte. The capacitance of EDLCs arises from the physical adsorption of ions and its efficiency is highly dependent on the size compatibility between the stored ions and carbon pores. HPC exhibits a dominant pore size distribution centred at ≈0.8 nm, which perfectly matches with the size of solvated Li^+ (≈0.8 nm) and BF_4^- (≈0.6 nm) ions in SUL (Uesugi et al. 2013; Piacentini et al. 2025). This precise match enables solvated Li^+ ions to readily enter the micropores of HPC and a high specific capacitance of 133 F g^{-1}, operating at the conventional voltage window between 0 and 2.7 V. By contrast, the commonly used tetraethylammonium cation (TEA^+) possesses a solvated diameter of 1.3–1.4 nm, far exceeding the dominant micropore size of the HPC with much decreased pore utilization, as evidenced by its markedly inferior discharge time in TEA^+-based electrolyte (Fig. S4) (Prehal et al. 2017). Even in the Li^+-based electrolyte, HPC still exhibits markedly higher capacitance than the other two reference carbon samples. The HPC_{insu} sample, with a dominant pore size of 0.6 nm, is too small for solvated Li^+ ions, whereas HPC_{exce}, with pores spanning 1–8 nm, is considerably larger than the solvated Li^+ dimension. These underscore the importance of size compatibility between pores and solvated ions for maximizing the charge storage. It should be noted that the delivered capacity of 133 F g^{-1} is ≈1.5 times higher than the commercial Kuraray YP-50F (90 F g^{-1}) whose pore structure does not match well with solvated Li^+ ions (Fig. S5).

To widen the operating voltage window of HPC, we first increased the concentration of $LiBF_4$ to formulate a highly concentrated electrolyte with enhanced electrochemical stability. Figure 4a and Fig. S6 show the cyclic voltammetry (CV) and galvanostatic charge–discharge (GCD) profiles. It is observed that all of them exhibit varying degrees of decomposition, accompanied by unsatisfied Coulombic efficiency (< 95%). The optimized formulation was found to be 4 M $LiBF_4$/SUL, affording a specific capacitance of 97.5 F g^{-1} with a Coulombic efficiency of 94% (Fig. 4b). At higher concentrations, specific capacitance (< 95 F g^{-1}) decreases significantly owing to large electrolyte viscosity, while at lower concentrations, electrolyte decomposition becomes more severe, resulting in even lower Coulombic efficiencies (< 85%).

To resolve this, we introduced TTE as a non-solvating diluent to form a weakly solvating electrolyte. TTE is miscible with SUL but does not coordinate with Li^+, thereby preserving the local highly concentrated Li^+-(SUL)n

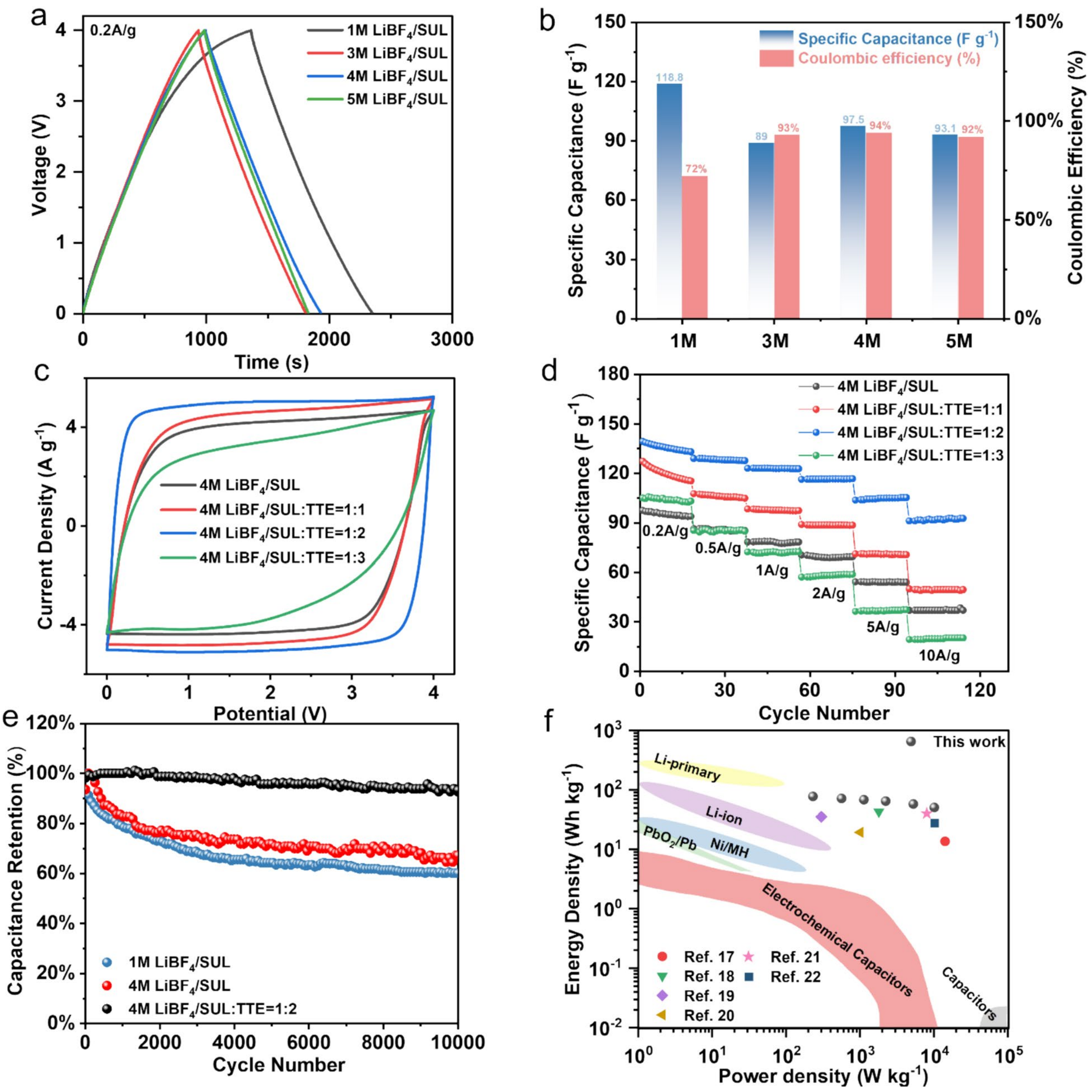

Fig. 4 **a** GCD profiles and **b** the corresponding specific capacitance and Coulombic efficiency of HPC in different LiBF$_4$ concentration electrolytes; **c** CV profiles; **d** long-term cyclability of HPC; **e** rate performance of HPC in electrolytes with different SUL/TTE volumetric ratios; **f** Ragone plot of HPC in comparison with previous reports

solvation structure while acting as a molecular "lubricant" to drastically lower the electrolyte viscosity and enhance the ionic conductivity. This design effectively retains the superior electrochemical stability of HCEs while overcoming their critical drawback of sluggish ion transport. The effectiveness of the enhanced voltage operation window with addition of TTE is implicit in the following: more rectangular CV curves (Fig. 4c), higher discharge time (Fig. S7), and better rate performance (Fig. 4d). At an optimized volume ratio of SUL:TTE = 1:2, HPC delivered the highest specific capacitance of 139 F g^{-1}. Even at a high current density of 10 A g^{-1}, HPC still had a high specific capacitance of 92 F g^{-1}. The high-rate performance is beneficial from the kinetically favourable electrode–electrolyte interface of HPC in the weakly solvating electrolyte, as revealed by the lowest charge-transfer resistance in Nyquist plots of HPC (Fig. S8). Moreover, we found that the fast charge and discharge

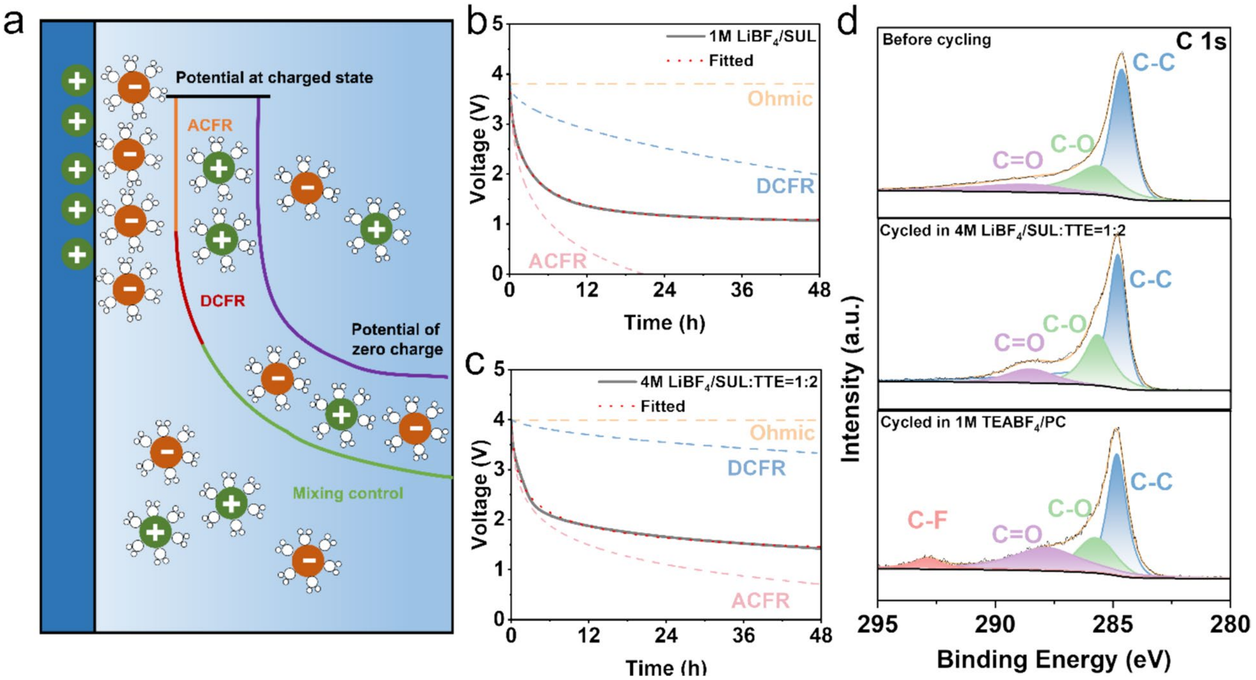

Fig. 5 Self-discharge kinetic analysis. **a** Schematic illustration of the self-discharge process at the electrode–electrolyte interface; **b**, **c** Curve fitting of the OCV profiles for HPC electrodes at different electrolyte systems; **d** Comparison of C 1 s XPS spectra of HPC electrodes cycled in 1 M TEABF$_4$/PC and 4 M LiBF$_4$/SUL:TTE (1:2) electrolytes after 10,000 cycles at a voltage window of 0–4 V

did not compromise the cycling stability. The HPC electrode retains over 90% of the initial capacitance after 10,000 cycles at 10 A g^{-1}, with a Coulombic efficiency close to unity (Fig. 4e and Fig. S9). This remarkable combination of high-rate capability and cyclability arises from the matched size compatibility between the tailored sub-nanometer pores of HPC and the weakly solvated electrolyte ions, which maximizes pore utilization and enables rapid ion transport. The advantage of this synergistic design is further highlighted in the Ragone plot (Fig. 4f), where the system achieves a maximum energy density of 77.4 Wh kg^{-1}—more than twice that of conventional symmetric capacitors (typically 25–35 Wh kg^{-1}) and positioning it among the highest-performing carbon-based devices reported to date (Yang et al. 2022; Wu et al. 2021; Liu et al. 2021; Zhang et al. 2025, 2022; Yin et al. 2020).

Self-discharge is a crucial challenge hindering the practical application of supercapacitors. It is a multistage process governed primarily by potential-driven (PD) ion redistribution and parasitic Faradaic reactions (FR), as shown in Fig. 5a. The initial rapid voltage drop is primarily controlled by PD ion redistribution where the high electric field forces ions to escape the electric double layer, followed by a slower and long-term voltage decay driven by parasitic Faradaic reactions (Conway et al. 1997). We probed these phenomena using both open-circuit voltage (OCV) decay and steady-state leakage current measurements, as shown in Fig. 5b, c and S10, 12. The OCV decay measurements clearly show that the capacitor using the weakly solvating electrolyte (4 M LiBF$_4$/SUL:TTE = 1:2) exhibits the slowest initial voltage drop at 4.0 V, suggesting that more stable and ordered Helmholtz interfacial layer is formed at HPC electrodes as a "dynamic drag" that effectively suppresses the PD ion redistribution at the initial process.

To quantitatively understand the long-term energy loss during the parasitic FR process, we further analyzed the OCV decay curves by fitting them to a well-established model (details in ESI) (Sun et al. 2024). It deconvolutes the voltage drop into three components by an initial Ohmic drop, diffusion-controlled faradaic reactions (DCFR), and activation-controlled faradaic reactions (ACFR). DCFR typically relates to the diffusion of redox impurities while ACFR involves slow and continuous parasitic reaction processes like solvent oxidation which are particularly critical in high-voltage operation in our case. By performing kinetic fitting on the OCV curves, we quantified the weakly solvating electrolyte system shows a markedly smaller ACFR contribution compared to the conventional (1 M LiBF$_4$/SUL) and HCE (4 M LiBF$_4$/SUL) electrolyte system designs (Figs. 5b, c and S11). This quantitatively confirms that the engineered weakly solvating electrolyte interface effectively suppresses the parasitic reaction rate. This is further corroborated by the steady-state leakage current measurements, in which the capacitor with the weakly solvating electrolyte demonstrates the lowest leakage current at both 2.7 and 4.0 V (Fig. S12). These results together demonstrate that the weakly solvating electrolyte design is beneficial for forming a more stable interfacial layer at the carbon electrode that effectively mitigates the self-discharge, even at elevated voltage operation.

To elucidate the origin of suppressed self-discharge in the weakly solvating electrolyte, XPS analysis was conducted on HPC electrodes after 10,000 cycles, compared with electrodes cycled in the conventional $TEABF_4$/PC electrolyte. As shown in Fig. 5d and Fig. S13, HPC electrodes cycled in $TEABF_4$/PC exhibit a pronounced C–F peak (~ 293 eV) and an increased C = O signal in the C 1s spectrum, indicative of significant electrolyte decomposition and irreversible Faradaic reactions. By contrast, HPC electrodes cycled in the weakly solvated 4 M $LiBF_4$/SUL:TTE electrolyte retain the original C–O and C = O functionalities, with no detectable C–F or other decomposition signals, demonstrating effective suppression of parasitic reactions and preservation of interfacial chemical integrity. This is also corroborated by electrochemical LSV measurements (Fig. S14), in which the conventional 1 M $TEABF_4$/PC electrolyte exhibits large oxidation current above ~2.5 V, whereas the TTE-containing weakly solvating electrolyte maintains a stable voltage window up to ~4.2 V. The broadened electrochemical stability window mitigates high-voltage oxidative decomposition, thereby reducing ACFR contributions in self-discharge.

4 Conclusions

In summary, we demonstrate a synergistic co-design strategy that successfully addresses the intrinsic voltage and self-discharge limitations of conventional supercapacitors. By integrating a hierarchical porous carbon derived from lignin with a tailored weakly solvating electrolyte, we simultaneously realize high specific capacitance and an unprecedented 4.0 V operating window, delivering an energy density of 77.4 Wh kg^{-1}, outstanding cycling stability over 10,000 cycles, and significantly suppressed self-discharge. The superior performance arises from two cooperative mechanisms: (i) geometric compatibility between solvated Li^+ ions and sub-nanometer pores, which maximizes charge storage, and (ii) a weakly solvating environment, enabled by the functional TTE diluent, which enhances ion transport while stabilizing the electrode–electrolyte interface and mitigating parasitic reactions at high potentials. Collectively, these results establish a viable pathway toward sustainable, high-energy supercapacitors and underscore weakly solvating electrolyte design as a promising strategy for next-generation energy storage devices.

Supplementary Information

The online version contains supplementary material available at https://doi.org/10.1007/s44246-025-00255-z.

Supplementary Material 1

Acknowledgements
This work was financially supported by the National Key Research and Development Program of China (No. 2023YFB4203704).

Authors' contributions

All authors contributed to the study conception and design. Yawen Tang and Hualin Ye performed the conceptualization and design of the study. Hualin Ye and Chenxin Cai performed supervision and funding acquisition. Data collection and analysis were performed by Shichao Zhang, Suyang Si, Keqi Zeng, and Shenglin Liu. The final draft of the manuscript was written by Shenglin Liu, Hualin Ye, and Feng Gong. All authors read and approved the final manuscript.

Funding
National Key Research and Development Program of China (No. 2023YFB4203704).

Data availability

The datasets used or analyzed during the current study are available from the corresponding author on reasonable requests.

Declarations

Competing interests

Xiangzhou Yuan is an editor of Carbon Research and was not involved in the editorial review, or the decision to publish, this article. All authors declare that there are no competing interests.

Author details
[1] Jiangsu Key Laboratory of New Power Batteries, Jiangsu Collaborative Innovation Center of Biomedical Functional Materials, School of Chemistry and Materials Science, Nanjing Normal University, Nanjing 210023, China. [2] Key Laboratory of Energy Thermal Conversion and Control of Ministry of Education, School of Energy and Environment, Southeast University, Nanjing 211189, Jiangsu, China. [3] Key Laboratory of Functional Polymers for Sustainability of Jiangsu, School of Energy and Environment, Southeast University, Nanjing 211189, China.

Received: 29 August 2025 Revised: 21 November 2025 Accepted: 17 December 2025

References

Blasio P, Elsborg J, Vegge T, Flores E, Bhowmik A (2024) CALiSol-23: Experimental electrolyte conductivity data for various Li-salts and solvent combinations. Sci Data 11(1):750. https://doi.org/10.1038/s41597-024-03575-8

Chun S-E, Evanko B, Wang X, Vonlanthen D, Ji X, Stucky GD et al (2015) Design of aqueous redox-enhanced electrochemical capacitors with high specific energies and slow self-discharge. Nat Commun 6(1):7818. https://doi.org/10.1038/ncomms8818

Conway BE, Birss V, Wojtowicz J (1997) The role and utilization of pseudocapacitance for energy storage by supercapacitors. J Power Sources 66(1):1–14. https://doi.org/10.1016/S0378-7753(96)02474-3

Ho JS, Borodin OA, Ding MS, Ma L, Schroeder MA, Pastel GR et al (2023) Understanding lithium-ion transport in sulfolane- and tetraglyme-based electrolytes using very low-frequency impedance spectroscopy. Energy Environ Mater 6(1):e12302. https://doi.org/10.1002/eem2.12302

Kim SC, Wang J, Xu R, Zhang P, Chen Y, Huang Z et al (2023) High-entropy electrolytes for practical lithium metal batteries. Nat Energy 8(8):814–826. https://doi.org/10.1038/s41560-023-01280-1

Kumar R, Mahalik JP, Silmore KS, Wojnarowska Z, Erwin A, Ankner JF et al (2020) Capacitance of thin films containing polymerized ionic liquids. Sci Adv 6(26):eaba7952. https://doi.org/10.1126/sciadv.aba7952

Liu K, Yu C, Guo W, Ni L, Yu J, Xie Y et al (2021) Recent research advances of self-discharge in supercapacitors: mechanisms and suppressing strategies. J Energy Chem 58:94–109. https://doi.org/10.1016/j.jechem.2020.09.041

Lu J, Zhang J, Wang X, Zhang J, Tian Z, Zhu E et al (2024) A review of advanced electrolytes for supercapacitors. J Energy Storage 103:114338. https://doi.org/10.1016/j.est.2024.114338

Pan C, Ji Y, Ren S, Lei T, Dong L (2025) Lignin-derived activated carbon as electrode material for high-performance supercapacitor. Molecules 30(1):89

Pech D, Brunet M, Durou H, Huang P, Mochalin V, Gogotsi Y et al (2010) Ultrahigh-power micrometre-sized supercapacitors based on onion-like carbon. Nat Nanotechnol 5(9):651–654. https://doi.org/10.1038/nnano.2010.162

Piacentini V, Simari C, Mangiacapre E, Pierini A, Gentile A, Marchionna S et al (2025) Aprotic electrolytes beyond organic carbonates: transport properties of LiTFSI solutions in S-based solvents. ChemSusChem 18(9):e202402273. https://doi.org/10.1002/cssc.202402273

Prehal C, Koczwara C, Jäckel N, Schreiber A, Burian M, Amenitsch H et al (2017) Quantification of ion confinement and desolvation in nanoporous carbon supercapacitors with modelling and in situ X-ray scattering. Nat Energy 2(3):16215. https://doi.org/10.1038/nenergy.2016.215

Ren X, Chen S, Lee H, Mei D, Engelhard MH, Burton SD et al (2018) Localized high-concentration sulfone electrolytes for high-efficiency lithium-metal batteries. Chem 4(8):1877–1892. https://doi.org/10.1016/j.chempr.2018.05.002

Sun L, Wu Z, Hou M, Ni Y, Sun H, Jiao P et al (2024) Unraveling and suppressing the voltage decay of high-capacity cathode materials for sodium-ion batteries. Energy Environ Sci 17(1):210–218. https://doi.org/10.1039/D3EE02817H

Uesugi E, Goto H, Eguchi R, Fujiwara A, Kubozono Y (2013) Electric double-layer capacitance between an ionic liquid and few-layer graphene. Sci Rep 3(1):1595. https://doi.org/10.1038/srep01595

Wu X, Li H, Yang X, Wang X, Miao Z, Zhou P et al (2021) Reduced graphene oxide hydrogel for high energy density symmetric supercapacitor with high operation potential in aqueous electrolyte. ChemElectroChem 8(22):4353–4359. https://doi.org/10.1002/celc.202101046

Yang J, Meng J, Zhang L, Chu K, Zong W, Ge L et al (2022) Dodecahedral carbon with hierarchical porous channels and bi-heteroatom modulated interface for high-performance symmetric supercapacitors. J Power Sources 549:232111. https://doi.org/10.1016/j.jpowsour.2022.232111

Ye H, Li Y (2023) A perspective on sulfur-equivalent cathode materials for lithium-sulfur batteries. Energy Lab 1(1):220003. https://doi.org/10.54227/elab.20220003

Yin J, Zhang W, Alhebshi NA, Salah N, Alshareef HN (2020) Synthesis strategies of porous carbon for supercapacitor applications. Small Methods 4(3):1900853. https://doi.org/10.1002/smtd.201900853

Yuan Z, Chen A, Liao J, Song L, Zhou X (2024) Recent advances in multifunctional generalized local high-concentration electrolytes for high-efficiency alkali metal batteries. Nano Energy 119:109088. https://doi.org/10.1016/j.nanoen.2023.109088

Zhang J, Li Q, Zeng Y, Tang Z, Sun D, Huang D et al (2023) Weakly solvating cyclic ether electrolyte for high-voltage lithium metal batteries. ACS Energy Lett 8(4):1752–1761. https://doi.org/10.1021/acsenergylett.3c00181

Zhang B, Xin Q, Chen S, Wang B, Li H, Wang Z et al (2025) Lithium-ion battery recycling relieves the threat to material scarcity amid China's electric vehicle ambitions. Nat Commun 16(1):6661. https://doi.org/10.1038/s41467-025-61481-y

Zhang W, Yin J, Jian W, Wu Y, Chen L, Sun M et al (2022) Supermolecule-mediated defect engineering of porous carbons for zinc-ion hybrid capacitors. Nano Energy 103:107827. https://doi.org/10.1016/j.nanoen.2022.107827

Zhang W, Yin J, Wang C, Zhao L, Jian W, Lu K et al (2021) Lignin derived porous carbons: synthesis methods and supercapacitor applications. Small Methods 5(11):2100896. https://doi.org/10.1002/smtd.202100896

Zhong C, Deng Y, Hu W, Qiao J, Zhang L, Zhang J (2015) A review of electrolyte materials and compositions for electrochemical supercapacitors. Chem Soc Rev 44(21):7484–7539. https://doi.org/10.1039/C5CS00303B

Publisher's Note